



Lithium secondary batteries working at very high temperature: Capacity fade and understanding of aging mechanisms

Lucille Bodenes ^a, Romain Naturel ^b, Hervé Martinez ^a, Rémi Dedryvère ^a, Michel Menetrier ^b, Laurence Croguennec ^b, Jean-Paul Pérès ^c, Cécile Tessier ^d, Florent Fischer ^{d,*}

^aIPREM/ECP (UMR 5254 CNRS), University of Pau, Hélioparc, 2 Av. Pierre Angot, 64053 Pau cedex 9, France

^bICM2B, Université de Bordeaux, ENSCBP, 33608 Pessac cedex, France

^cSAFT, rue Georges Leclanché, BP 1039, 86000 Poitiers cedex 9, France

^dSAFT, 111-113 bd. Alfred Daney, 33074 Bordeaux cedex, France

HIGHLIGHTS

- Li(Ni,Mn,Co)O₂/carbon lithium-ion batteries were cycled at +85 °C and +120 °C for 15 days.
- Good stability of chosen electrochemistry at +85 °C.
- XPS, XRD, SEM and NMR were used to identify main aging mechanisms.
- Positive electrode binder PVDF was identified as the main aging root cause.
- Evolution of the SEI composition was quantified between +85 °C and +120 °C.

ARTICLE INFO

Article history:

Received 26 October 2012

Received in revised form

15 February 2013

Accepted 22 February 2013

Available online 4 March 2013

Keywords:

Lithium-ion batteries

High temperature

SEI

XPS

NMR

ABSTRACT

Li(Ni,Mn,Co)O₂/carbon lithium-ion batteries designed to work at high temperature exhibit good performances for cycling at 85 °C but a strong impedance increase for cycling or storage at 120 °C. The effects of high temperature on the aging process of positive electrode's binder, electrodes/electrolyte interfaces and positive active material were investigated by bulk and surface analysis techniques: X-ray diffraction, ⁷Li and ¹⁹F Nuclear Magnetic Resonance, Scanning Electron Microscopy and X-ray Photo-electron Spectroscopy. The main phenomenon observed at 120 °C is a migration of PVDF binder from the outer part of the positive electrode which thus shows a bad Li reintercalation. Binder migration results in the formation of a PVDF layer at the extreme surface of the positive electrode, and in its diffusion and deposition on the surface of the negative electrode. Several changes in the composition of the Solid Electrolyte Interphase (SEI) were also evidenced between a cycle at 60 °C and cycling at 85 °C and 120 °C. Disappearance of carbonate species disappearance and increase of inorganic species, which both together may also affect battery's performance. Though, since the battery can undergo 25 cycles at 120 °C, Li(Ni,Mn,Co)O₂ seems to be an appropriate material for high temperature cycling.

© 2013 Elsevier B.V. All rights reserved.

1. Introduction

Batteries able to work at relatively high temperature (between +85 °C and +150 °C) are required for some specific applications with very aggressive environment. As examples of applications, we can cite the oil drilling and all downhole operations which need Measurement While Drilling (MWD) tools working at very high temperatures. There is also an interest of such batteries in heat sterilizable applications for the medical field. Today, lithium

thionyl chloride (Li–SOCl₂) primary batteries are able to work with good performances in such environment (from –40 °C to +150 °C) [1]. However, for the oil drilling applications, these primary cells must be changed at the end of their discharge. Therefore, there is an added value to use secondary batteries capable to work even with a limited number of cycles in such conditions, which will lower maintenance tasks for the user. Moreover, use of rechargeable batteries has a positive impact on environment because lower amount of raw materials is required for a similar function. Lithium-ion secondary batteries thus appear as a promising alternative to the traditional primary lithium batteries, but performances of lithium-ion cells with conventional organic electrolyte solvents were rarely investigated at temperatures higher than 100 °C.

* Corresponding author.

E-mail address: florent.fischer@saftbatteries.com (F. Fischer).

Most commercial lithium-ion batteries manufactured today are well known for their good performances at room temperature and at temperatures below 60 °C [2]. Several studies have already reported results on the aging of various cell components after high temperature tests: on characterizations of the carbon negative electrode performances upon cycling at +80 °C [3,4], on the Solid Electrolyte Interphase (SEI) compositions on carbon after storage at 80 °C [5], on the aging of positive active material of $\text{LiNi}_{1-x-y}\text{Co}_x\text{Al}_y\text{O}_2$ type after 80 °C cycling [6,7], on the electrochemical performances of lithium-ion batteries based on $\text{LiCo}_{1/3}\text{Ni}_{1/3}\text{Mn}_{1/3}\text{O}_2$ and $\text{Li}_4\text{Ti}_5\text{O}_{12}$, and tested up to +95 °C [8] and on the capacity fade with LiCoO_2 and graphite cells at +55 °C [9]. Other evaluations of innovative positive or negative active materials are also reported, for example: $\text{Li}_2\text{Ti}_3\text{O}_7$ material for the negative electrode up to +70 °C [10], spinel LiMn_2O_4 at +75 °C [11] or LiFePO_4 at +90 °C [12] for the positive electrode.

In all these studies, strong capacity fading is usually reported for storage and/or cycling at temperatures between +60 °C and +100 °C [8–10,12]. Degradation of active material is frequently proposed as a root cause of this high fading (either metal dissolution [13] or local structural changes [7]), but most of the time, problems related to the SEI and interfaces degradations are highlighted on both electrodes (in terms of stability, composition or thickening) [3,5,11,14].

Tests at higher temperature (above 100 °C) are scarcer and usually require a real breakthrough in cell electrochemistry compared to standard commercial lithium-ion cells.

An electrochemical cell composed of LiFePO_4 as cathode, LiTFSI as molten salt electrolyte and metallic lithium as anode was described to be able to work at temperature up to 300 °C [15], but less than 10 cycles were reported at 250 °C.

Very promising results were presented with an innovative electrolyte composed of molten salt (Li/K/Cs TFSI): 50 cycles were performed at +150 °C with only 5% of capacity loss and a coulombic efficiency close to 100% [16]. The electrochemical cell was composed of LiFePO_4 as positive active material and lithium metal as negative. However, one disadvantage of this system is that the electrolyte salt can only work at temperature above 146 °C (corresponding to the melting point of this eutectic composition). Ionic liquids were also tested with a $\text{TiO}_2\text{-B}$ negative active material versus lithium metal [17]. Piperidinium based ionic liquids were the best choice and lead to 20 cycles at +120 °C.

Up to 170 cycles at +100 °C were also obtained with a liquid electrolyte (composed of ethylene carbonate with LiBOB), LiFePO_4 as positive and metallic lithium as negative [18]. Recently, a new electrochemistry based on grafted copolymer as electrolyte: (poly(oxyethylene) methacrylate-g-poly(dimethyl siloxane) (POEM-g-PDMS) doped with lithium triflate) was also presented to be efficient to work at +120 °C for 30 cycles with a LiFePO_4 positive but still with a lithium negative electrode [19].

SAFT has been working on this topic since 2004, using for the first time graphite at 120 °C and not metallic lithium as negative electrode [20–23].

The present work intends to identify aging mechanisms of Li-ion cells with graphite as active material at such high temperatures up to 120 °C and to participate to the improvement of lithium-ion batteries stability at high temperature. For this purpose, laboratory prototype lithium-ion cells with standard organic-based electrolytes together with carbon material as negative were evaluated at +85 °C and +120 °C. Effects of high temperature tests were studied, not only on active materials, but also on the other components of the cell such as binders or on the Solid Electrolyte Interphase (SEI) that formed either on the positive or on the negative side. Various analytical techniques were used: surface analysis techniques like X-ray photoelectron spectroscopy (XPS), X-ray Fluorescence (XRF) for metallic detection on aged electrodes, SEM and bulk analysis techniques like X-ray diffraction (XRD) for

active material characterizations and Nuclear Magnetic Resonance (NMR).

2. Experimental

2.1. Cell preparation and aging tests

Electrochemical tests were performed in prototype cells. Negative electrodes were prepared by coating an aqueous ink made of a mixture of carbons as the active material, and carboxymethyl cellulose (CMC) and styrene butadiene rubber (SBR) respectively as thickener and binder, on a copper foil current collector. Positive electrodes were prepared by coating an aluminum foil current collector with a slurry of $\text{LiNi}_{1/3}\text{Mn}_{1/3}\text{Co}_{1/3}\text{O}_2$, poly(vinylidene fluoride) (PVdF) binder and conductive carbon, in N-methyl-2-pyrrolidone (NMP). The electrolyte is a mixture of cyclic carbonates (propylene carbonate and ethylene carbonate) containing LiPF_6 . Electrodes were assembled into 2 Ah prototype cylindrical cells. Charge–discharge cycling tests at elevated temperatures (+60, +85 and +120 °C) were performed using Digatron battery tester and appropriate climate chambers. Cycling tests were carried out at C/5 rate in the range of 2.7–4.1 V. The behavior of 3 cells after 15 days of cycling or storage in 3 different high temperature conditions have been compared to a reference cell that was only aged at 60 °C for 1 day (the various test conditions are summarized in Table 1):

- The reference cell was subjected to two cycles at +60 °C: this cell will be referenced as B1.
- After the same two initial cycles at 60 °C, one cell was cycled at +85 °C between 2.7 and 4.1 V for 15 days: this cell will be referenced as B2.
- After the same two initial cycles at 60 °C, one cell was cycled at +120 °C between 2.7 and 4.1 V for 15 days: this cell will be referenced as B3.
- After the same two initial cycles at 60 °C, one cell was stored at +120 °C for 15 days with an initial voltage charge at 3.9 V at 60 °C: this cell will be referenced as B4.

Internal resistances of the cells (in $\text{m}\Omega$) were followed during cycling. Internal resistances were calculated for each cycle using the voltage drop between the end of the charge (open circuit voltage) and after 5 s of discharge at C/5, and calculated using Ohm's law ($R = \Delta U / \Delta I$).

2.2. Analysis techniques

After the electrochemical tests described above, cells were discharged at room temperature down to 2.5 V at a C/10 rate. Cell cans were opened using appropriate cutting tools in an argon-filled dry box. The positive and negative electrodes were carefully separated from the rest of the battery components in the dry box. Samples of electrodes were collected and then washed with a large excess of Di

Table 1
Description of aging tests.

Cell reference	B1	B2	B3	B4
Test conditions	60 °C: 2 cycles at C/5	60 °C: 2 cycles at C/5 followed by 26 cycles at 85 °C between 2.7 and 4.1 V	60 °C: 2 cycles at C/5 followed by 29 cycles at 120 °C between 2.7 and 4.1 V	60 °C: 2 cycles at C/5 then charge at 3.9 V at 60 °C: storage for 15 days

Methyl Carbonate (DMC) solvent to remove the electrolyte. They were dried carefully under primary vacuum at room temperature before carrying out the characterizations. The sample to be analyzed was recovered from the electrode film as described hereafter for each case.

2.2.1. XRD

The positive electrode materials recovered from these high temperature batteries were characterized by X-ray diffraction (XRD) using a Siemens D5000 diffractometer equipped with a detector using energy discrimination and Cu K α radiation, in the 10–80° (2 θ_{Cu}) range, with steps of 0.02° (2 θ_{Cu}) and a constant counting time of 16 s. Before their XRD analysis, in addition to the washing process described just above, these positive electrode samples were soaked in glove box, under intermittent stirring, during 4 days at room temperature in a large excess of NMP in order to dissolve PVdF, remove the material from the current collector and recover a loose powder. That powder was then carefully dried under vacuum and sieved at 40 μm before being maintained under argon in a specific tight sample-holder, to prevent any contact with ambient atmosphere during the acquisition and thus, any evolution. The profile matching refinement of the XRD patterns was performed using the Fullprof software [24].

2.2.2. SEM

Changes in the morphology of the positive and negative electrodes were observed by scanning electron microscopy (SEM) using a Hitachi S4500 field emission microscope with an accelerating voltage of 4.8 kV. The samples, electrodes recovered after washing in a large excess of DMC, were coated under primary vacuum and during 20 s with a thin layer of palladium in order to prevent any charge accumulation on their surface. No separation of the active material powder from the electrode and especially from the binder was performed, as for characterization by XRD, because here the first goal of scanning electron microscopy was really to observe possible changes in the distribution between the different constituents of the electrodes and also in the nature/texture of the surface and grain boundaries.

X-ray Fluorescence (XRF) measurements on electrodes were performed using a PW2400 PANALYTICAL XRF spectrometer. The X-ray source was a Rhodium anode. Analysis was performed on a circular sample of 27 mm diameter.

2.2.3. ^7Li and ^{19}F NMR

The electrode material was recovered from the electrode film by scraping in an argon-filled glove box, and inserted into a 2.5 mm NMR rotor. This procedure showed that only part of the electrodes cycled at 120 °C was recovered this way. The other part of the electrode remained strongly adherent to the current collector. Another procedure was therefore also adopted, using NMP to separate the electrode from the current collector, similarly to the procedure used for recovering the samples for XRD. At room temperature, NMP may partly dissolve the PVdF binder, but the process used leads anyway to a redeposition upon drying. This redeposition is very probably nonhomogenous, leading to possibly PVdF-rich regions.

^7Li and ^{19}F MAS NMR spectra were recorded using a Bruker Avance 300 spectrometer with a 2.5 mm MAS probe spinning at 30 kHz. For ^7Li (116 MHz), a Hahn echo pulse sequence synchronized with the rotor period was used (90° pulse length: 2.4 μs , recycling delay 10 s). The spectra are referenced to an external LiCl 1 M solution (0 ppm). For ^{19}F (282 MHz), a single pulse sequence (90° pulse length: 1.6 μs , recycle delay: 10 s) was used. The spectra are referenced to CFCl_3 (0 ppm) using $\text{C}_6\text{H}_5\text{CF}_3$ as a secondary reference (−63, 72 ppm).

2.2.4. XPS

XPS measurements were carried out with a Kratos Axis Ultra spectrometer, using a focused monochromatized Al K α radiation ($\hbar\nu = 1486.6$ eV). The XPS spectrometer was directly connected to an argon dry box through a transfer chamber, to avoid moisture/air exposure of the samples. For the Ag 3d5/2 line the full-width at half maximum (Fwhm) was 0.58 eV under the recording conditions. Portions of the electrodes recovered and rinsed as described above were used without further processing. The analyzed area of the samples was 300 $\mu\text{m} \times 700 \mu\text{m}$. The analyzing depth of the XPS is about the first 5 nm of the surface of the electrode. Peaks were recorded with constant pass energy of 20 eV. The pressure in the analysis chamber was around 5×10^{-7} Pa. Short acquisition time spectra were recorded before and after each regular experiment to check that the samples did not suffer from degradation under the X-ray beam during measurements. Peak assignments were made with respect to reference compounds analyzed in the same conditions, namely LiPF_6 , LiF , Li_2CO_3 , $\text{CH}_3\text{OCO}_2\text{Li}$ [25–27]. The binding energy scale was calibrated from the hydrocarbon contamination using the C 1s peak at 285.0 eV. Core peaks were analyzed using a nonlinear Shirley-type background. The peak positions and areas were optimized by a weighted least-square fitting method using 70% Gaussian, 30% Lorentzian lineshapes. Quantification of the chemical species at the surface by XPS is given in atomic percent (at.%) taking into account all the elements of the considered species, and is performed on the basis of Scofield's relative sensitivity factors. For example, 4 at.% of LiF = 2 at.% of Li (Li 1s peak at 56 eV) + 2 at.% of F (F 1s peak at 685 eV).

3. Results and discussion

3.1. Electrical tests

Figs. 1 and 2 report cycling results of B2 cells (cycling at +85 °C) and B3 cells (cycling at +120 °C). Discharge capacity evolutions are plotted in Fig. 1, as a function of the number of cycles, together with charge discharge profiles during high temperature cycling for both series. Evolution of internal resistance as a function of cycle number is plotted in Fig. 2. Table 2 summarizes electrochemical results: A moderate 7.5% loss of capacity was measured after 26 cycles at +85 °C and a 22% loss was obtained after 29 cycles at 120 °C. These results are rather good, considering the high temperatures of these tests. Other studies using graphite-based negative electrodes and lithium layered oxide as positive materials report also a significant fading at temperatures below 100 °C: for example, 4.3% of capacity loss after 50 cycles at +55 °C with LiCoO_2 [9] or 10% capacity loss after 500 cycles at +60 °C with $\text{Li}(\text{Ni},\text{Co})\text{O}_2$ [28].

However, it is clear that for these high temperatures, the internal resistance increase and the capacity loss remain significant upon cycling compared to results usually reported at room temperature with lithium secondary cells (7% of energy loss after 1300 cycles at room temperature on standard Saft 41 Ah cells at C/3 [2]).

At +85 °C, the impedance increase measured after 26 cycles is +100% and it is +1115% associated with the 22% capacity loss after 29 cycles at +120 °C. Therefore, strong side reactions are suspected to occur in the cell and more significantly at +120 °C compared to +85 °C. Fig. 3 shows the evolution of the Open Circuit Voltage for the B4 cell during storage for 15 days at +120 °C after an initial charge up to 3.9 V at 60 °C. The voltage decreases from 3.90 V to 3.68 V, which might indicate an accelerated aging of the battery during this storage test, probably linked with side reactions.

Analyses of electrodes recovered from these 4 cells were performed in order to understand the main side reactions that lead to this high impedance increase. The goal is to identify the aging mechanisms occurring at temperature above +60 °C.

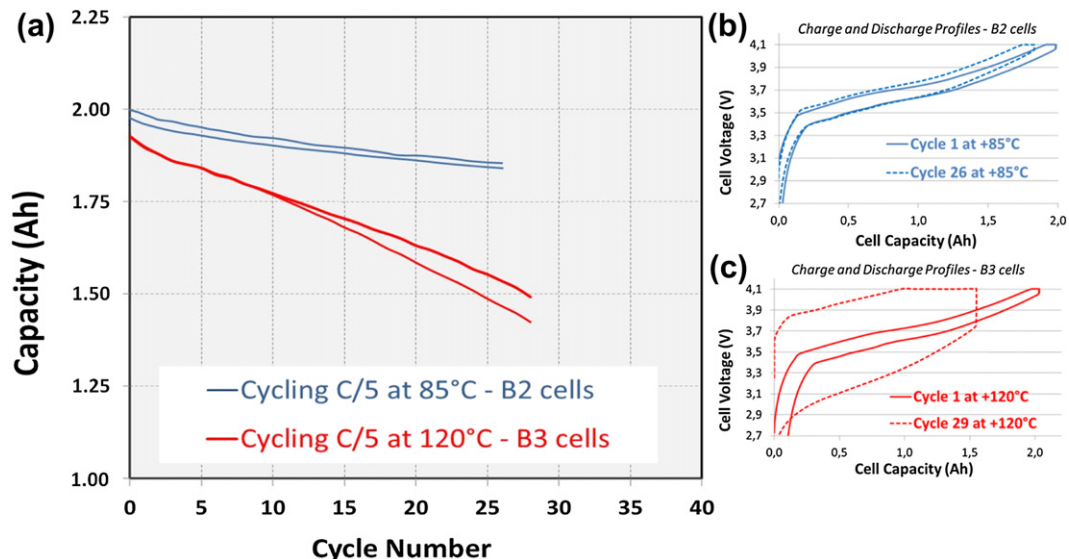


Fig. 1. Cells tested at high temperature (B2 at 85 °C and B3 at 120 °C) in cycling at C/5 between 2.7 V and 4.1 V (with galvanostatic mode + potentiostatic mode at end of charge voltage). a. Discharge capacity (Ah) vs. cycle number. b. Charge and discharge profiles of B2 cells (cycle 1 and cycle 26 at +85 °C): cell voltage (V) as a function of cell capacity (Ah). c. Charge and discharge profiles of B3 cells (cycle 1 and cycle 29 at +120 °C): cell voltage (V) as a function of Cell capacity (Ah).

The part 2 of this paper is focused on aging of the positive active material, while the part 3 is dedicated to the aging of the binder. Finally, the part 4 deals with aging of the passivation layer formed at the negative electrode/electrolyte interface (SEI).

3.2. Aging of the positive electrode active material

All the XRD patterns can be indexed in the $R\text{-}3m$ space group as expected for a single phase of layered $\alpha\text{-NaFeO}_2$ type (Fig. 4). They were refined using full pattern matching refinements, for all of them a good minimization of the difference between the experimental data and the calculated pattern is obtained. For all the materials recovered from these high temperature batteries, after cycling or after storage, the cell parameters remain significantly different from those observed for the pristine material (Table 3):

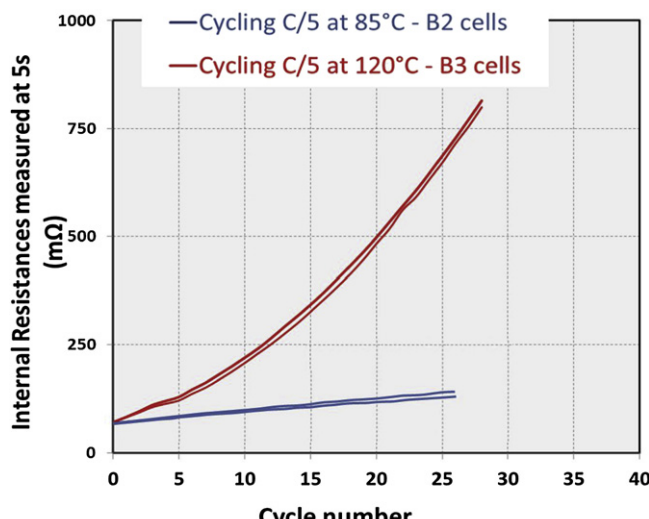


Fig. 2. Internal resistance as a function of the number of cycles for cells tested at high temperature (B2 at 85 °C and B3 at 120 °C) in cycling at C/5 between 2.7 V and 4.1 V (with galvanostatic mode + potentiostatic mode at end of charge voltage).

a_{hex} is smaller whereas c_{hex} is larger, as expected after a discharge in full cell vs. graphite, where materials do not recover their LiMO_2 pristine composition [29]. As a result the transition metal ions remain more oxidized than in the initial state, in good agreement with a shorter M–M (a_{hex}) distance. The electrostatic repulsions between the oxygen layers on both sides of the interslab space remain also stronger due to a smaller amount of screening (lithium) ions, inducing an increase of the interslab distance ($c_{\text{hex}}/3$). From these XRD analyzes we can conclude that no significant modifications of the bulk material are observed whatever the cycling conditions (temperature, or cycling versus storage). The state of reintercalation (and the deviation of the observed cell parameters with the pristine ones) appears only dependent on the depth of the battery discharge before recovering the electrode and not on the aging of the material.

^7Li NMR spectra for the electrodes B1, B2 and B3 are plotted in Fig. 5 in comparison with that for the pristine electrode. In Fig. 5a, the spectra are plotted in absolute intensity scale, referred to the amount of material. The broad signal observed arises from the Li in the active material, which experiences drastic hyperfine interactions from the electron spins on neighboring Ni and Mn [30]. Due to the broad distribution of the possible local environments around Li in the compound, the signal is not separated into spinning sidebands in the present measurement conditions and cannot therefore be analyzed further. However, the figure shows strong changes in its magnitude that can be analyzed as follows. Since, due to the width of the signal discussed above, a Hahn echo sequence is required to record it, the magnitude of the signal recorded is very sensitive to the T2 relaxation time. When the latter becomes close

Table 2
Summary of electrochemical results for B2 and B3 cells.

Cycle number	Capacity loss (%)/1st cycle at high temperature	Average capacity loss per cycle (%)/1st cycle at high temperature	Impedance increase (%)/1st cycle at high temperature
Cell B2 (85 °C)	26	7.5%	0.29%
Cell B3 (120 °C)	29	22%	0.76%

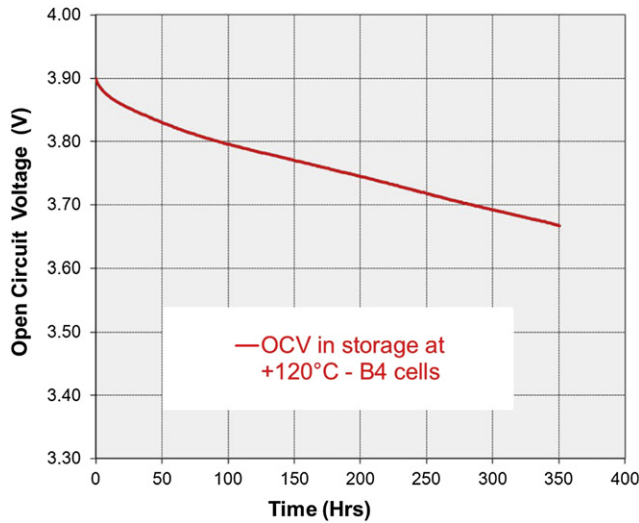


Fig. 3. Open circuit voltage evolution of B4 cell during storage at +120 °C after an initial charge at C/5 and 60 °C with constant current until 3.9 V.

to the refocusing delay of the echo pulse sequence (synchronized to one rotor period i.e. 33.33 μ s), the magnitude of the signal strongly decreases. One major cause for the decrease of T2 can be Li mobility in this timescale [31]. Therefore, when the Li amount in the NMC material decreases even slightly, the magnitude of the broad NMR signal drastically decreases. Fig. 5a therefore shows that the amount of Li in the material is less than 1 for all the electrodes (recovered after the cycle at 60 °C). This is expected since the discharge process performed before dismantling the cell cannot lead to full reintercalation, and is in agreement with the XRD observations above. Fig. 6 shows a schematic diagram of the positive electrode after cycling at 120 °C: the usual sampling process for NMR analysis is to scrape the electrode to remove it from the current collector. In the case of the electrode cycled at 120 °C, as seen on Fig. 6, only part 1 of the electrode is easily removed by scraping, while part 2 remains adherent to current collector. Two kinds of analyzes are then performed for the positive electrode cycled at 120 °C: part 1 is analyzed after being scraped, and the whole electrode is analyzed by recovering it with NMP (same process as XRD). It appears clearly that the reintercalation is much better for the part of the electrode recovered using NMP. This suggests that

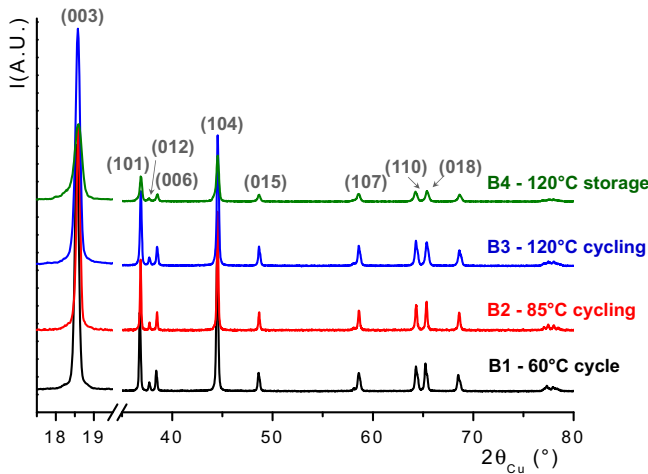


Fig. 4. X-ray diffraction patterns ($\lambda_{K\alpha_{Cu}} = 1.5406 \text{ \AA}$) of NMC positive electrode material recovered from B1, B2, B3 and B4 cells.

Table 3

Cell parameters determined from XRD analysis for the different positive electrode materials.

Sample name	$a_{\text{hex.}} (\text{\AA})$	$c_{\text{hex.}} (\text{\AA})$	$V_{\text{cell}} (\text{\AA}^3)$
Pristine material	2.8589(9)	14.232(1)	100.74(1)
B1 – 60 °C formation cycle	2.8550(1)	14.263(1)	100.68(1)
B2 – 85 °C cycling	2.8527(3)	14.276(2)	100.62(2)
B3 – 120 °C cycling	2.8522(3)	14.286(4)	100.65(4)
B4 – 120 °C storage	2.8541(2)	14.311(1)	100.96(1)

part 1 of the electrode has suffered more severe degradation than part 2, which will be analyzed further in this paper when addressing the NMR characterization of the PVdF binder. Another important observation is that this is specific to the B3 electrode (cycled at 120 °C), since the scraped 85 °C electrode does not show this drastic decrease of Li reintercalation.

Fig. 5a also shows a narrow signal close to 0 ppm, with its set of spinning sidebands. This corresponds to Li in a diamagnetic layer at the surface of the material [32,33]. An expansion plot of the isotropic signal for the series of electrodes is given in Fig. 5b. The amount of Li in the layer increases after the 60 °C cycle and the cycling at 85 °C, with, however, little change in the nature of the signal. After cycling at 120 °C, the signal for the scraped part of the electrode (part 1) is rather different in nature from the former ones and appears weaker in magnitude. Again, for the “NMP recovered” part of the same electrode, the signal shape is strongly altered. Considering the resolution of the spectra and the complexity of the

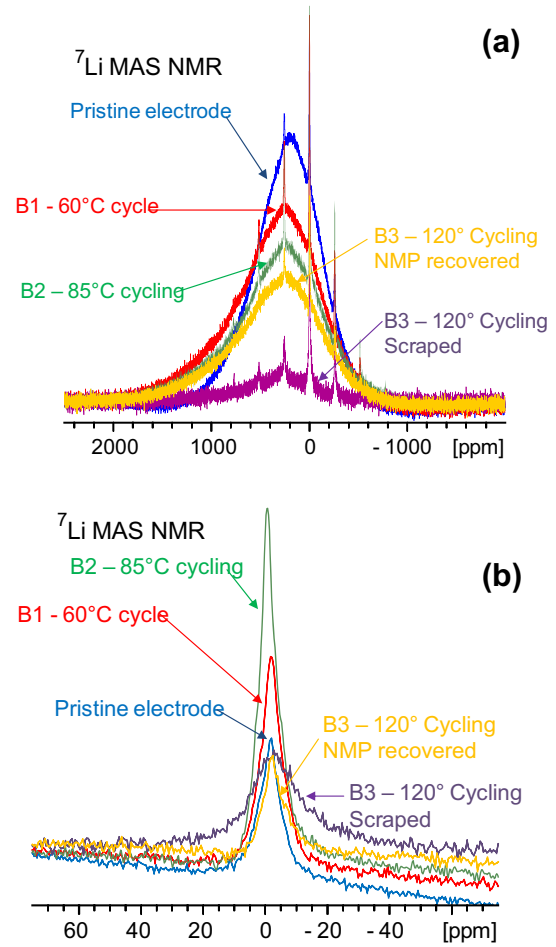


Fig. 5. (a) ^7Li NMR spectra of positive electrodes: pristine electrode and B1, B2 and B3 samples. (b) Expansion plots of the isotropic signal of surface Li.

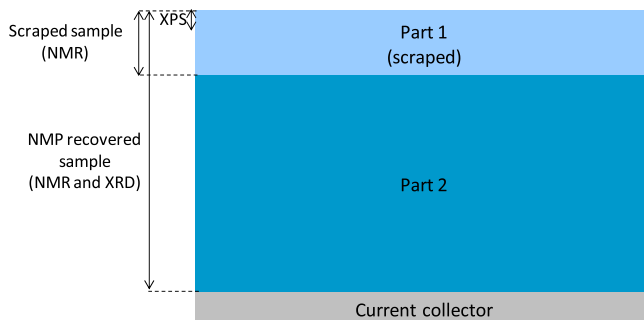


Fig. 6. Schematic diagram of the different parts of the positive electrode after cycling or storage at 120 °C, and corresponding scales of analysis techniques.

phenomenon observed, it appears unreasonable to extract further information. Nonetheless, it is clear that there is more Li in the surface layer for the electrodes cycled at 60 and 85 °C, and that the nature of the Li in the surface layer is markedly different for the electrode cycled at 120 °C.

XPS measurements were performed on positive electrodes to investigate their extreme surface composition. Li 1s, Ni 3p, Co 3p and Mn 3p core peaks could be observed by XPS: **Table 4** reports % M/(%Ni + Mn + Co) ratios measured at the top 5 nm of the positive electrode by XPS for the fresh electrode, and for those cycled at 60 °C and 85 °C (M = Ni, Co or Mn). These results are in good agreement with the formula of the active material $\text{Li}_x(\text{Ni}_{1/3}\text{Mn}_{1/3}\text{Co}_{1/3})\text{O}_2$, which shows that cycling at 85 °C does not alter the stoichiometry at the surface of the active material. For cycling and storage at 120 °C, the metals and oxygen peaks related to the active material are not detectable due to the modification of the surface of the positive electrode, as commented later. For the same reason and contrary to ${}^7\text{Li}$ NMR results (because of bulk analysis method), lithium in the surface layer is not detected by XPS after cycling or storage at 120 °C.

Besides, the XPS study of the extreme surface and XRF study of the bulk of the negative electrode reveal that small amounts of metals (Ni, Co and Mn) are deposited at the surface of the negative electrode during cycling. The corresponding amounts of transition metals detected at the surface of the negative electrode by XPS (atomic percentage) and XRF (mass percentage) are reported in **Table 5**. Note that in this case, the quantities measured by XRF are lower compared to XPS since XRF probes the whole electrode thickness (bulk analysis), while XPS probes the extreme surface of the electrodes where the metals are located. The observation of transition metals on the negative electrode can be explained by the dissolution of the active material of the positive electrode due to the presence of HF in the electrolyte [34]. The dissolved metals are then deposited by reduction at the negative electrode surface [35].

These amounts are not larger after cycling at 85 °C than after cycling at 60 °C. Manganese is the metal which is detected in larger amounts by XPS. This trend is confirmed by X-ray Fluorescence Spectrometry (XRF). After cycling or storage at 120 °C, the atomic percentage of manganese detected slightly increases and is still

Table 5

Amounts of Ni, Co, Mn measured by XPS (atomic percentage) and by XRF (mass ratio in ppm) for the negative electrode.

XPS	Ni (%)	Co (%)	Mn (%)
B1 (60 °C)	0.10	0.10	0.13
B2 (85 °C)	Not detected	Not detected	0.14
B3 (120 °C)	0.05	0.05	0.22
B4 (120 °C)	<0.01	Not detected	0.31
XRF	Ni (ppm)	Co (ppm)	Mn (ppm)
B1 (60 °C)	20	Not detected	Not detected
B2 (85 °C)	Not detected	Not detected	Not detected
B3 (120 °C)	50	Not detected	250
B4 (120 °C)	40	Not detected	50

higher than those of cobalt and nickel. The amounts of nickel detected by XRF also increase, contrary to XPS measurements. This variation is probably again related to the difference of analyzing depth between the two techniques, and may reveal a diffusion of Ni atoms in the bulk of the negative electrode upon cycling. Cycling or even storage at 120 °C seems to slightly enhance the dissolution of metals of the positive active material, which might be explained either by a larger concentration of HF in the electrolyte at this temperature in agreement with Yang et al. [36] and/or by an enhanced kinetics of dissolution due to higher temperature.

However, the quantities of dissolved metals detected are rather low. Indeed, they are similar to those observed at 20 °C for cobalt dissolution in LiCoO_2 /graphite systems, for which 0.4% of cobalt is detected by XPS at the extreme surface of the graphite electrode after long cycling (400 cycles) in a voltage range of 2.7–4.2 V [37]. For the system studied in the present paper and considering the small amount of dissolved metals, the performance fading of batteries at 85 °C and 120 °C cannot be attributed to the dissolution of NMC material.

Several conclusions about the aging of the positive active material at high temperature can thus be drawn from the results of the previous analyzes:

- XRD and ${}^7\text{Li}$ NMR (NMP recovered sample) analyzes indicate that no major modification of the bulk material occurs for high temperature cycling or storage.
- ${}^7\text{Li}$ NMR (scraped sample) results also show that the Li intercalation is drastically lower in the part 1 of the positive electrode than in the bulk (part 2) after cycling at 120 °C which is not observed after cycling at 85 °C.
- XPS and XRF studies reveal a minor dissolution phenomenon of metals from the positive active material (that deposit at the surface of the negative electrode).

3.3. Aging of positive electrode binder (PVdF)

The XPS C 1s spectrum of the fresh positive electrode (**Fig. 7**) displays an intense peak at 284.8 eV, which is assigned to carbon from the conductive additive, carbon black. Two other peaks with similar intensities are observed at 286.4 and 290.9 eV which, by comparison with the C 1s spectrum of pure PVdF also displayed on **Fig. 7**, can be assigned to the PVdF binder of the positive electrode. They are attributed to carbon atoms in $-(\text{CH}_2-\text{CF}_2)-$ and to $-(\text{CH}_2-\text{CF}_2)-$ respectively, in agreement with the different electronegativity of the elements (H and F).

The C 1s spectra of electrodes cycled at 60 °C (B1) and at 85 °C (B2) are similar to the spectrum described above, with the appearance of two peaks at 287.8 and 289.2 eV, attributed to new components with carbons in mono- and di-oxygenated environments [25]. This result suggests that the formation of a passivating

Table 4

Ni, Mn, and Co metal-to-metal ratios measured by XPS at the surface of positive electrodes from Ni 3p, Mn 3p and Co 3p spectra.

	%Ni	%Mn	%Co
	% (Ni + Co + Mn)	% (Ni + Co + Mn)	% (Ni + Co + Mn)
Fresh electrode	0.34	0.33	0.33
B1 – 60 °C	0.32	0.36	0.32
B2 – 85 °C	0.35	0.35	0.30

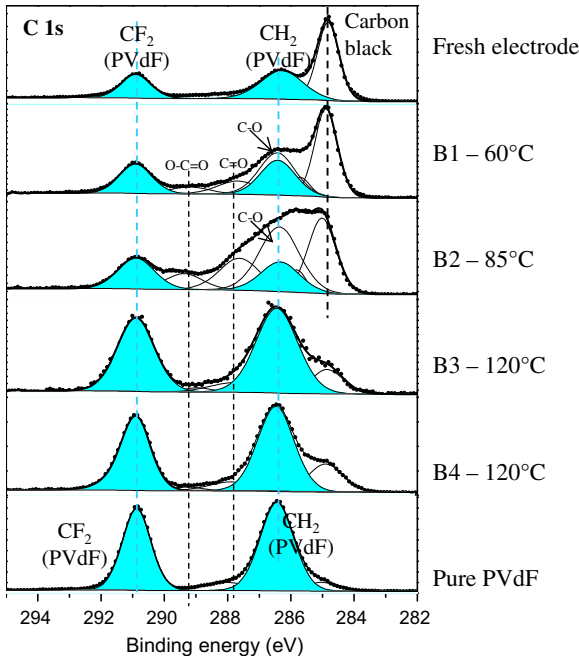


Fig. 7. C 1s XPS spectra of positive electrodes: pristine electrode, B1, B2, B3 and B4 samples and of pure PVdF polymer.

film at the surface of the positive electrode resulting from degradation of the electrolyte's solvents has occurred. However, the carbon black peak is still visible and evidences that the passivating film is very thin (less than 5 nm thick), or discontinuous.

C 1s spectra of electrodes cycled or stored at 120 °C (B3 and B4) are different from those described above: they exhibit a predominance of peaks assigned to PVdF (at 286.4 and 290.9 eV) among other components. C 1s spectra at 120 °C are actually very similar to the pure PVdF spectrum.

Table 6 shows the amounts (atomic percentages) of PVdF measured at the surface of each positive electrode from C 1s and F 1s spectra (at.% of PVdF = at.% of carbon from CH₂ and CF₂ groups + at.% of fluorine from CF₂ groups of PVdF). The atomic percentage of PVdF measured by XPS at the surface of the starting electrode is equal to 45%. Note that this value is much higher than the actual percentage of PVdF in the electrode (below 10%) as the binder covers the active material particles (surface effect). The amounts of PVdF measured at the surface of positive electrodes recovered from batteries cycled at 60 °C (42%) and 85 °C (28%) are lower than at the surface of the raw electrode. For the electrode cycled at 85 °C (B2), this can be explained by the appearance of additional species deposited in the passivation layer. This hypothesis is confirmed by an increase of the atomic percentage of oxygen from surface species (from 10 to 18%), coming from the passivation layer. However, the atomic percentage of PVdF is almost doubled on the positive electrode B3 after cycling at 120 °C (71%) and reaches 67% on the electrode stored at 120 °C after a charge at 3.9 V (B4).

Table 6

Atomic percentages of PVdF measured by XPS at the surface of positive and negative electrodes.

At. % of PVdF	Fresh electrode	B1			
		60 °C	85 °C	120 °C	120 °C
Surface of positive electrodes	45%	42%	28%	71%	67%
Surface of negative electrodes	Not detected	Not detected	6%	22%	20%

These analyses clearly show a migration of the positive electrode binder PVdF at the surface of the electrode upon the temperature increase: at 120 °C, PVdF covers the surface of the positive electrode.

¹⁹F MAS NMR spectra for the B1, B2 and B3 electrodes compared to that for the pristine electrode are plotted in Fig. 8a.

These spectra are dominated by a parasitic broad signal from PTFE parts of the NMR probe used. This signal furthermore impedes the baseline correction process required by the first-order phase correction inherent to the single-pulse sequence used. However, one can clearly observe additional signals that arise from the PVdF binder of the electrode, in the form of a set of spinning sidebands. The isotropic signal is around -100 ppm, on the very steep portion of the parasitic static signal, which makes it very difficult to observe. Therefore, we focus on the first positive spinning sideband around +10 ppm, and Fig. 8b shows an expansion of this portion of the spectra, with a baseline correction process and a scaling factor corresponding to the relative amount of material in the NMR rotors. The first observation from this expansion plot is that the amount of PVdF in the B1 electrode (after the 60 °C cycle) as well as in B2 (after the 85 °C cycling) appears higher than in the pristine electrode. Since all corresponding NMR samples were obtained by scraping, this suggests that the PVdF binder has partly migrated toward the surface of the electrode during the 60 °C cycle and the 85 °C cycling, and/or has migrated through the electrolyte in a more or less

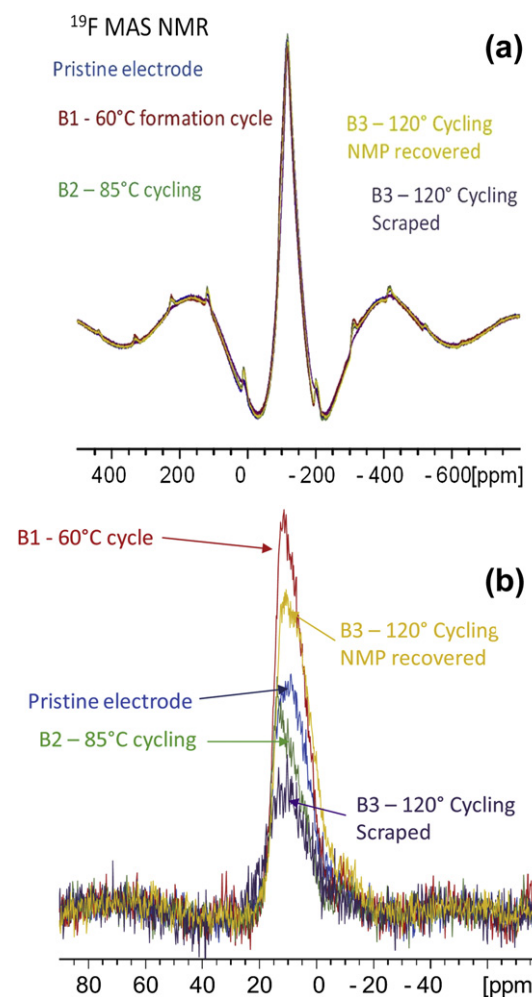


Fig. 8. (a) ¹⁹F NMR spectra of positive electrodes: pristine electrode and B1, B2 and B3 samples. (b) Expansion plots of the first positive spinning band.

solvated state. The important observation from Fig. 8b is that the amount of PVdF in the part 1 of the B3 electrode (recovered after the 120 °C cycling) appears very low. We have of course checked that the recycle delay used for these NMR experiments leads to quantitative observation. Our suggested explanation is that, in the outer part of the electrode (part 1), most of the PVdF binder has migrated to the surface of the electrode and remained adherent on the separator-side when dismantling the cell. It furthermore seems that the nature of the signal of the remaining PVdF is altered, but we cannot discuss further this point here. Another, more surprising, information is that the amount of PVdF for the “NMP-recovered” sample of the same B3 electrode appears higher than in the pristine electrode. We have no explanation for this fact, but, considering that NMP was used to separate the electrode film from the current collector, it is likely that some PVdF has been dissolved and deposited during this process, in a nonhomogeneous way (see Experimental section) which makes the analysis rather delicate.

From the SEM enlargement given on the left of Fig. 9 (x 2000), the aggregates of the active material appear slightly more covered after the cycle at 60 °C. This deposit could be attributed to PVdF in agreement with the above XPS and NMR analysis. Nevertheless, from the larger enlargement given on the right of Fig. 9 (x 25,000), the surface of the primary particles remains almost free from any additional degradation layer. After the cycling performed at 85 °C, the primary particles are still observed within the agglomerates, but their surface is slightly covered, whereas the grain boundaries are partially filled and less visible. With the increase of the temperature up to 120 °C, the electrode is covered by a thick layer of PVdF, in good agreement with the XPS results: neither the primary particles nor the shape of the aggregates can be observed anymore. This reveals significant changes within the microstructure of the electrode: the distribution of the binder is not homogeneous anymore as shown by its migration to the surface of the electrode.

The analysis of the negative electrode by XPS also provides information about the positive electrode binder PVdF.

The C 1s spectrum (Fig. 10) of the fresh negative electrode displays a narrow main peak at 284.1 eV assigned to graphite. The second peak at 285.0 eV is assigned to the characteristic peak of SBR binder and to hydrocarbon contamination [26]. The two other peaks observed at 286.7 and 288.5 eV are attributed to CO- and CO₂-like carbon atoms in the CMC binder respectively [38].

The graphite component is no longer detectable on the C 1s spectrum of the electrode cycled at 60 °C (B1): as expected, an SEI film was formed at the surface of the negative electrode, thicker than the XPS analysis depth (about 5 nm).

Concerning the C 1s core peak of the negative electrode cycled at 85 °C (B2), the main difference compared to the 60 °C reference sample is the additional peak appearing at high binding energy (290.9 eV). This binding energy corresponds to carbon in a CF₂ environment as observed on the C 1s spectra of the positive electrode and can be assigned in the same way to CF₂ from the PVdF binder. Moreover, the F 1s spectrum (not shown here) displays a peak at 687.7 eV, corresponding to the same attribution. The relative intensities of these peaks (ratio F(CF₂)/C(CF₂) about 2) allows to definitely assign this component to CF₂ of PVdF.

After cycling or storage in the charged state at 120 °C (B3 and B4), the C 1s peak attributed to CF₂ increases significantly with respect to the other components.

These observations of C 1s core peaks of negative electrodes cycled or stored at elevated temperatures confirm previous conclusions about the effect of high temperature on the positive electrode binder PVdF. Table 6 reveals the amount of PVdF measured by XPS at the surface of negative electrodes, and reports that the PVdF binder of the positive electrode can be found in small amounts (6%) at the surface of the negative electrode after cycling

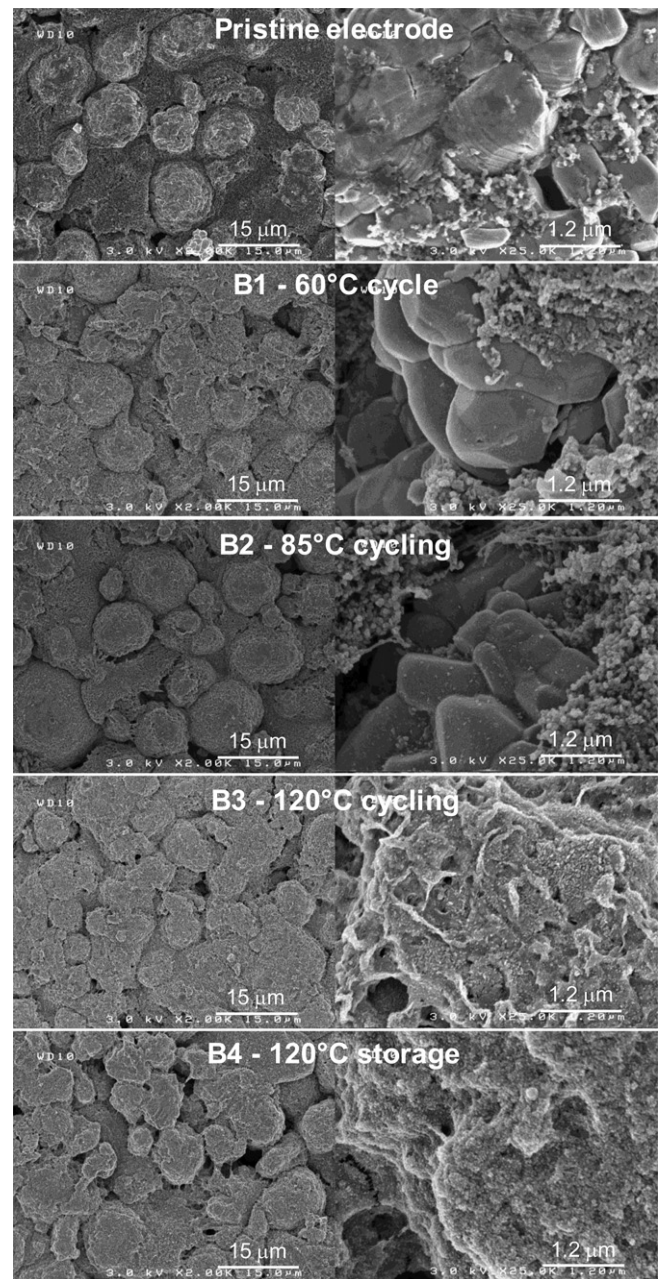


Fig. 9. SEM images of positive electrodes: pristine electrode and B1, B2, B3 and B4 samples.

at 85 °C. However, at 120 °C this quantity reaches 20%, and is characteristic of a significant deposit of binder coming from the positive electrode on the negative electrode at this temperature, across the separator. A more or less complete dissolution process of PVdF in the electrolyte therefore occurs at high temperature.

As the binder migration (at elevated temperature) occurs in the case of stored as well as cycled electrodes, this phenomenon is not due to successive charges and discharges.

The main results about aging of the positive electrode's binder PVdF are:

- XPS analysis and SEM images show a major covering of positive electrodes cycled at 120 °C.
- ¹⁹F MAS NMR spectra (scraped samples) reports a very low amount of PVdF in the part 1 of the positive electrode after cycling at 120 °C compared to part 2.

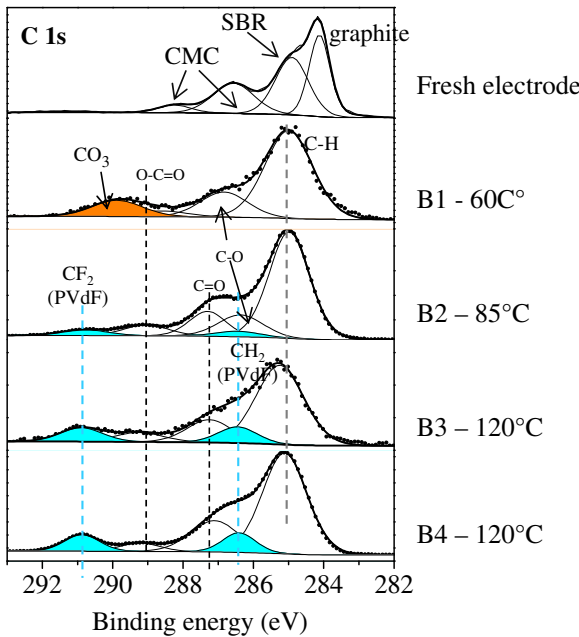


Fig. 10. C 1s XPS core peaks of negative electrodes for pristine electrode for B1, B2, B3 and B4 sample.

- XPS analysis of the negative electrodes reveals the migration of positive electrodes' binder PVdF and its diffusion in the electrolyte through the separator.

Conclusions about the aging of the active material and of the PVdF binder of positive electrode lead to a possible mechanism occurring at the positive electrode during cycling at 120 °C: the PVdF binder may migrate from the part 1 of the positive electrode (scraped part) to the surface of the electrode in contact with the separator. This would explain the small amount of PVdF measured in the scraped sample (part 1) by ¹⁹F NMR analysis, and the major covering of the positive electrode's surface by PVdF observed by XPS and SEM. The PVdF binder that migrates at the surface of the positive electrode also diffuses in the electrolyte through the separator and is deposited at the negative electrode's surface during cycling at 120 °C. This hypothesis is consistent with a bad Li reintercalation in the part 1 of the electrode, probably related to a bad cohesion due to the binder migration.

However, the degradation of the positive electrode at 120 °C only concerns the part 1 of the electrode, while most of the bulk (part 2) is well reintercalated with a good cohesion ensured by the PVdF binder.

A schematic diagram of the positive electrode after cycling at 120 °C is suggested on Fig. 11.

3.4. Carbon electrode & SEI

The description of C 1s core peaks of negative electrodes (Fig. 10) shows that a passivating film is formed during the first cycle at 60 °C, as the graphite peak from the active material is not detectable (Fig. 10 – B1). This film on the carbon particles is thicker than the XPS analysis depth (about 5 nm). Compared to the fresh electrode, a new peak is displayed at 289.9 eV, and can be assigned to a carbon in a CO₃ environment, which is consistent with the formation of lithiated carbonates (Li₂CO₃ or ROCO₂Li) resulting from the solvent degradation [39]. Unlike the C 1s spectrum of the fresh electrode, the two characteristic peaks of carbon in C–O and O=C=O–like environments (at 286.6 and 289.1 eV) are not attributed to CMC binder as

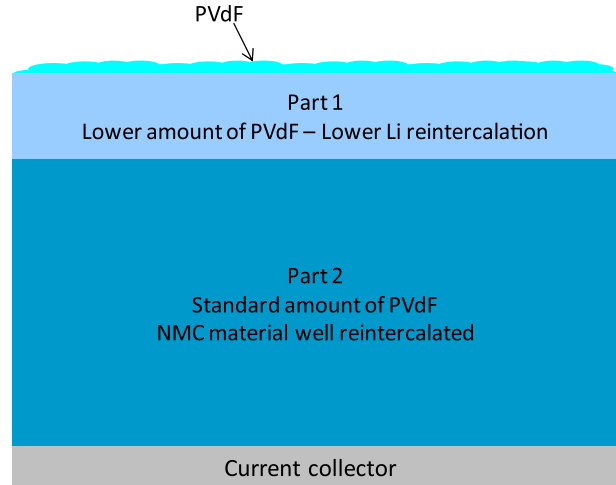


Fig. 11. Schematic diagram of the positive electrode after cycling at 120 °C.

the surface of the electrode is covered by a surface film. Note that the CMC binder is covered due to its reactivity toward the electrolyte [38]. These two peaks can thus be assigned to new organic species also resulting from the solvent components' decomposition process, forming the SEI. The environments of carbon atoms in the SEI after one cycle at 60 °C are as follows: CH₂, C–O, O=C=O, CO₃. The quantity of lithiated carbonate species (calculated thanks to carbon, oxygen and lithium atomic percentages) accounts for about 40% of the first 5 nm of the surface layer (Table 7).

After cycling at 85 °C for 15 days, the C 1s spectrum (Fig. 10 – B2) is close to the spectrum previously described for one cycle at 60 °C. The peak associated with graphite is still not detected. Then, the passivating film still exists at 85 °C. The additional peak appearing at 290.9 eV has been attributed to the PVdF binder coming from the positive electrode in Section 3. The characteristic peak of carbon in CO₃-like environments is not detected on the negative electrode after cycling at 85 °C. Disappearance of XPS peaks attributed to lithiated carbonate species might be attributed to the temperature increase rather than to longer cycling as several studies reported their presence after long cycling at room temperature (LiCoO₂/graphite, 440 cycles between 2.7 and 4.1 V) [37] and at 60 °C (LiFePO₄/graphite, 200 cycles between 2.5 and 3.7 V) [40]. In the case of 85 °C cycling, lithiated carbonates deposited at 60 °C may be covered by other species preferably formed at high temperature, or may dissolve in the electrolyte.

As observed previously concerning the binder, the peak attributed to CF₂ on C1s spectra shows a strong increase with respect to the other components for cycling or storage in the charged state at 120 °C (Fig. 10 – B3, B4). As observed for cycling at 85 °C, carbonates species are not detected on the surface of electrodes cycled or stored at 120 °C.

Other XPS spectra, namely F 1s, P 2p, O 1s and Li 1s, not shown here, allow to determine the amounts of inorganic species present in the 5 nm surface layer of the negative electrode, as reported in Table 7: compared to the negative electrode of the battery cycled at

Table 7

Atomic percentages of inorganic species detected by XPS at the surface of the negative electrodes.

	B1 60 °C	B2 85 °C	B3 120 °C	B4 120 °C
LiF	2%	4%	8%	10%
LiPF ₆	6%	Not detected	Not detected	Not detected
Phosphates/ fluorophosphates	7%	25%	21%	17%
Carbonate species	40%	Not detected	Not detected	Not detected

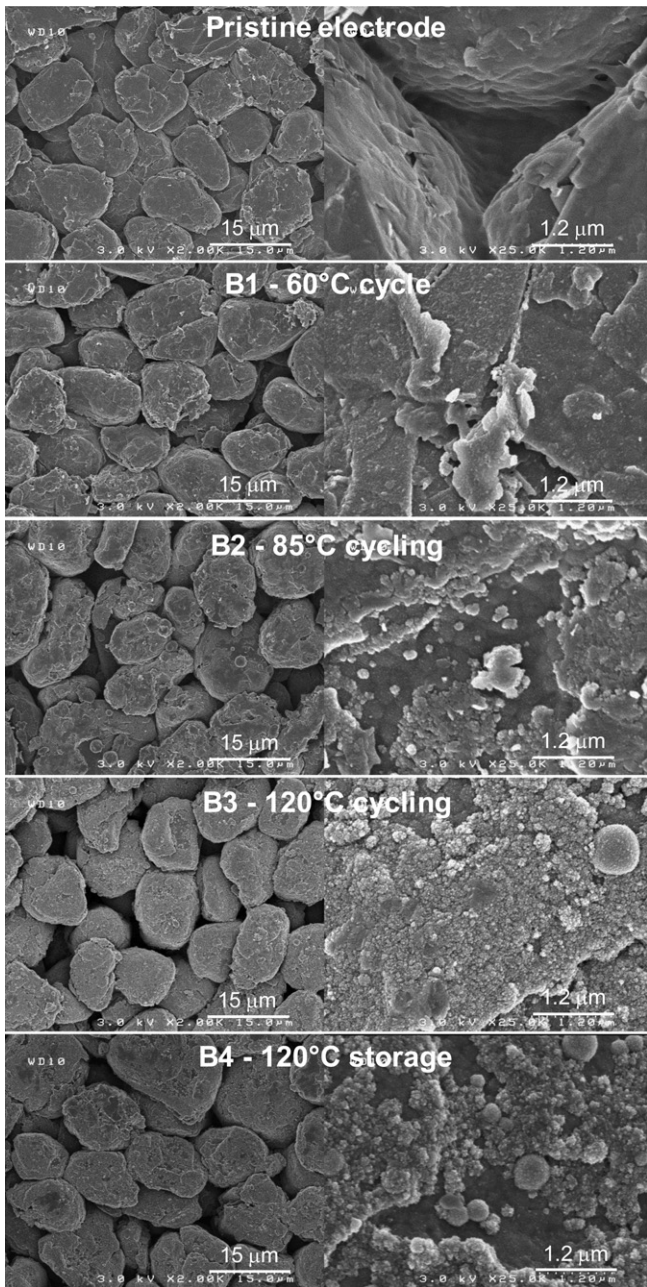


Fig. 12. SEM images of negative electrodes: pristine electrode and B1, B2, B3 and B4 samples.

60 °C, the atomic percentage of LiF measured by XPS increases from 2 to 4%, and the lithium salt LiPF₆ is no longer detected. This result is consistent with the fact that LiF is formed from the degradation of LiPF₆, which is enhanced by high temperature. Table 7 exhibits an increase of the atomic percentage of phosphate/fluorophosphates species, which are also LiPF₆'s degradation products. Then, this result is consistent with the temperature increase. Changes between cycling at 60 and 85 °C are significant as phosphates/fluorophosphates atomic percentage increases from 7 to 25%. As observed during cycling at 85 °C, LiPF₆ is not detected on the surface of negative electrodes after cycling or storage at 120 °C. The amount of LiF increases compared to cycling at 85 °C. However, the atomic percentage of phosphates/fluorophosphates slightly decreases.

As a summary, between 60 and 85 °C, the amount of phosphates/fluorophosphates sharply increases while carbonate species

are no longer detected. LiF tends to be more deposited at 85 °C. However, the major changes occur between 85 and 120 °C, with a strong increase in PVdF amounts and disappearance of carbonate species. Those changes in the chemical composition of the SEI may modify the properties of the passivating film and thus partly explain the decline of the electrochemical performances of the battery at 120 °C.

The SEM observations of the negative electrode (Fig. 12) show that the state of the surface at the negative is immediately modified after the cycle at 60 °C as expected from the formation of the commonly observed Solid Electrolyte Interphase (SEI). After a cycling at 85 °C, the surface of the particles remains very similar to that observed at 60 °C. On the contrary, an increase of the temperature up to 120 °C induces the formation of a thicker SEI layer with also spherical particles ("balls"). Using Energy Dispersive X-ray analyzes we have shown that as expected the elements detected in the SEI (next to carbon) are fluorine, oxygen and phosphorus (lithium being not detected), but also that the "balls" observed on Fig. 12 are rich in fluorine (~80 wt%) and oxygen (~16 wt%) (estimation done after removal of carbon contribution).

4. Conclusions

Lithium-ion batteries based on carbon (negative electrode) and NMC (positive electrode) have been studied after cycling at 85 °C or cycling or storage at 120 °C, in order to examine the influence of very high temperature cycling or storage on battery aging. The batteries exhibit good performances for 85 °C cycling, and a reasonable capacity fading at 120 °C (22%) for 29 cycles. However, batteries cycled at 120 °C exhibit a strong impedance increase, most likely caused by side reactions related to high temperature.

The main phenomenon identified at 120 °C is caused by the positive electrode binder PVdF: it migrates from part 1 of the positive electrode (near the surface) to create a layer mainly composed of PVdF (about 70% in the first 5 nm) at the surface of the electrode. The binder also diffuses into the electrolyte and through the separator and is deposited at the surface of the negative electrode. Decohesion of the positive electrode is suspected in the part 1 from which PVdF migrates, leading to a bad Li reintercalation in the active material as observed by ⁷Li NMR.

However, in a major part of the positive electrode (part 2), XRD analysis shows that the active material NMC is well reintercalated. Analysis of negative electrodes shows a slight dissolution of the positive active material in the electrolyte. These results confirm that NMC is an appropriate material for high temperature cycling.

Several changes in the SEI are reported for 85 and 120 °C cycling: carbonates species disappear from the surface layer and an increase of inorganic species (phosphates and LiF) is observed. This modification of the SEI composition layer may affect its properties and thus the battery's performances, and partly explains the capacity loss and the impedance increase at high temperature, in addition to the binder migration to the electrode surface of the positive electrode.

Acknowledgments

The authors wish to thank ANR (Agence Nationale de la Recherche) Stock-E program (ANR-09-STOCK-E-05) for financial support.

References

- [1] SAFT, in: SAFT Product Specification of Primary High Temperature Lithium Battery (LSH 20-150) (2009). Available from: http://www.saftbatteries.com/doc/Documents/primary/Cube655/LSH%2020_150_0209.a7f37738-2b50-4084-89de-2cea69882952.pdf.

[2] SAFT, in: SAFT Product Specification of VLM Cells (Medium Power Lithium-ion Cells) (2005). Available from: http://www.saftbatteries.com/doc/Documents/liion/Cube572/54042_VLM_cells_0305.d0d8d859-9174-42f2-84b2-19632e4b0760.pdf.

[3] E. Markevich, E. Pollak, G. Salitra, D. Aurbach, *Journal of Power Sources* 174 (2007) 1263–1269.

[4] L. Bodenes, R. Dedryvère, H. Martinez, F. Fischer, C. Tessier, J.-P. Pérès, *Journal of the Electrochemical Society* 159 (2012) A1738–1746.

[5] A.M. Andersson, K. Edstrom, *Journal of the Electrochemical Society* 148 (2001) A1100–A1109.

[6] S. Muto, Y. Sasano, K. Tatsumi, T. Sasaki, K. Horibuchi, Y. Takeuchi, Y. Ukyo, *Journal of the Electrochemical Society* 156 (2009) A371–A377.

[7] Y. Kojima, S. Muto, K. Tatsumi, H. Kondo, H. Oka, K. Horibuchi, Y. Ukyo, *Journal of Power Sources* 196 (2011) 7721–7727.

[8] Yabuuchi, T. Ohzuku, *Journal of Power Sources* 146 (2005) 636–639.

[9] P. Ramadas, B. Haran, R. White, B.N. Popov, *Journal of Power Sources* 112 (2002) 606–613.

[10] S. Ma, H. Noguchi, *Journal of Power Sources* 161 (2006) 1297–1301.

[11] K. Araki, N. Sato, *Journal of Power Sources* 124 (2003) 124–132.

[12] S.S. Zhang, K. Xu, T.R. Jow, *Journal of Power Sources* 159 (2006) 702–707.

[13] C. Wang, A.J. Appleby, F.E. Little, *Journal of Electroanalytical Chemistry* 497 (2001) 33–46.

[14] M.C. Smart, B.V. Ratnakumar, J.F. Whitacre, L.D. Whitcanack, K.B. Chin, M.D. Rodriguez, D. Zhao, S.G. Greenbaum, S. Surampudi, *Journal of the Electrochemical Society* 152 (2005) A1096–A1104.

[15] D. Muñoz-Rojas, J.-B. Leriche, C. Delacourt, P. Poizot, M.R. Palacín, J.-M. Tarascon, *Electrochemistry Communications* 9 (2007) 708–712.

[16] A. Watarai, K. Kubota, M. Yamagata, T. Goto, T. Nohira, R. Hagiwara, K. Ui, N. Kumagai, *Journal of Power Sources* 183 (2008) 724–729.

[17] J. Mun, Y.S. Jung, T. Yim, H.Y. Lee, H.-J. Kim, Y.G. Kim, S.M. Oh, *Journal of Power Sources* 194 (2009) 1068–1074.

[18] F. Mestre-Aizpuru, S. Hamelet, C. Masquelier, M.R. Palacín, *Journal of Power Sources* 195 (2010) 6897–6901.

[19] Q. Hu, S. Osswald, R. Daniel, Y. Zhu, S. Wesel, L. Ortiz, D.R. Sadoway, *Journal of Power Sources* 196 (2011) 5604–5610.

[20] F. Bonhomme, P. Biensan, D. Germond, J.M. Laluque, Patent Application EP1619741, 2004.

[21] F. Bonhomme, D. Germond, J.M. Laluque, P. Biensan, International Meeting on Lithium Batteries, Biarritz, France, 2006. Abstract N°462.

[22] F. Fischer, D. Germond, J.-P. Pérès, P. Biensan, International Meeting on Lithium Batteries, Tianjin, China, 22–28 June 2008. Abstract N°552.

[23] SAFT, SAFT Product Specification of Rechargeable High Temperature Lithium-ion Battery (VL 25500-125) (2009). Available from: http://www.saftbatteries.com/doc/Documents/liion/Cube572/VL%2025500-125_0309.7cd5da82-492e-4001-b430-9454b5ea37fa.pdf.

[24] J. Rodriguez-Carvajal, Laboratoire Léon Brillouin (2004). <http://www-lbb.cea.fr/fullweb/powder.htm>.

[25] S. Leroy, H. Martinez, R. Dedryvère, D. Lemordant, D. Gonbeau, *Applied Surface Science* 253 (2007) 4895–4905.

[26] R. Dedryvère, S. Laruelle, S. Grugéon, L. Gireaud, J.-M. Tarascon, D. Gonbeau, *Journal of the Electrochemical Society* 152 (2005) A689–A696.

[27] R. Dedryvère, L. Gireaud, S. Grugéon, S. Laruelle, J.-M. Tarascon, D. Gonbeau, *The Journal of Physical Chemistry B* 109 (2005) 15868–15875.

[28] Y. Itou, Y. Ukyo, *Journal of Power Sources* 146 (2005) 39–44.

[29] N. Tran, L. Crogueennec, C. Labrugère, C. Jordy, P. Biensan, C. Delmas, *Journal of the Electrochemical Society* 153 (2006) A261–A269.

[30] C.P. Grey, N. Dupré, *Chemical Reviews* 104 (2004) 4493–4512.

[31] C. Chazel, M. Ménétrier, L. Crogueennec, C. Delmas, *Inorganic Chemistry* 45 (2006) 1184–1191.

[32] M. Ménétrier, C. Vaysse, L. Crogueennec, C. Delmas, C. Jordy, F. Bonhomme, P. Biensan, *Electrochemical and Solid-State Letters* 7 (2004) A140–A143.

[33] N. Dupré, J.-F. Martin, D. Guyomard, A. Yamada, R. Kanno, *Journal of the Electrochemical Society* 156 (5) (2009) C180.

[34] S.F. Lux, I.T. Lucas, E. Pollack, S. Passerini, M. Winter, R. Kostecki, *Electrochemistry Communications* 14 (2012) 47–50.

[35] J. Vetter, P. Novak, M.R. Wagner, C. Veit, K.C. Müller, J.O. Besenhard, M. Winter, M. Wohlfahrt-Mehrens, C. Vogler, A. Hammouche, *Journal of Power Sources* 147 (2005) 269–281.

[36] L. Yang, M. Takahashi, B. Wang, *Electrochimica Acta* 51 (2006) 3228–3234.

[37] S. Verdier, L. El Ouatani, R. Dedryvère, F. Bonhomme, P. Biensan, D. Gonbeau, *Journal of the Electrochemical Society* 154 (2007) A1088–A1099.

[38] L. El Ouatani, R. Dedryvère, J.B. Ledeuil, C. Siret, P. Biensan, J. Desbrières, D. Gonbeau, *Journal of Power Sources* 189 (2009) 72–80.

[39] D. Aurbach, B. Markovsky, A. Shechter, Y. Ein-Eli, H. Cohen, *Journal of the Electrochemical Society* 143 (1996) 3809–3820.

[40] L. Castro, R. Dedryvère, J.B. Ledeuil, J. Breger, C. Tessier, D. Gonbeau, *Journal of the Electrochemical Society* 159 (2012) A357–A363.